Seismoelectric signals produced by mesoscopic heterogeneities: spectroscopic analysis of fractured media

M. Rosas-Carbajal [1], D. Jougnot [2], J. G. Rubino [3], L. Monachesi [4], N. Linde [5], K. Holliger [5]

[1]Institut de Physique du Globe de Paris, Sorbonne Paris Cité, CNRS UMR 7154, Université Paris Diderot, Paris, France
[2]Sorbonne Universités, UPMC Université Paris 06, CNRS, EPHE, UMR 7619 METIS, Paris, France
[3]CONICET, Centro Atómico Bariloche - Comisión Nacional de Energía Atómica, S. C. de Bariloche, Argentina
[4]CONICET, Instituto de Investigación en Paleobiología y Geología, Universidad Nacional de Río Negro, Argentina
[5]Applied and Environmental Geophysics Group, Institute of Earth Sciences, University of Lausanne, Lausanne, Switzerland

Key Points:

- Mesoscopic compressibility contrasts cause wave-induced fluid flow
- Measurable seismoelectric signals are generated by wave-induced fluid flow
- Energy-based approach to study the seismoelectric conversion in fracture networks

Corresponding author: M. Rosas-Carbajal, rosas@ipgp.fr

Abstract

In fluid-saturated porous rocks, the presence of mesoscopic heterogeneities such as, for example, fractures, can produce measurable seismoelectric signals. The conversion of mechanical energy into electromagnetic energy is related to wave-induced fluid flow (WIFF) between the heterogeneities and the embedding background. This physical mechanism is a well-known cause of seismic attenuation, which exhibits a strong frequency dependence related to rock physical and structural properties. Consequently, seismoelectric signals arising from WIFF are also expected to depend on various material properties, such as the background permeability and fracture characteristics. We present analytical and numerical approaches to study the effects of mesoscopic heterogeneities on seismoelectric signals. We develop an energy-based approach to quantify the total energy converted to seismoelectric signals at the sample scale. In particular, we apply our theoretical framework to fractured rock sample models and study the spectral signature of the resulting seismoelectric signals. This study highlights the influence of the mechanical and hydraulic properties, as well as the geometrical characteristics, such as degree of fracture connectivity, of the probed medium on the resulting seismoelectric signal.

1 Introduction

One common assumption in seismoelectric studies is that the involved media are homogeneous at the sub-wavelength scale. However, most geological environments typically contain mesoscopic heterogeneities, that is, heterogeneities larger than the pore size but smaller than the dominant seismic wavelength. In presence of contrasts in elastic compliance, the stress field associated with a propagating seismic wave produces a pore fluid pressure gradient and, consequently, wave-induced fluid flow (WIFF), which results in energy dissipation due to viscous friction. Indeed, WIFF is currently considered to be one of the major causes of seismic wave attenuation in the upper part of the Earth's crust [e.g. *Müller et al.*, 2010]. For this reason, efforts directed towards a better understanding of WIFF involving theoretical analyses [e.g., *Müller and Gurevich*, 2005], laboratory measurements [e.g., *Batzle et al.*, 2006; *Tisato and Madonna*, 2012; *Subramaniyan et al.*, 2014], and numerical simulations [e.g., *Masson and Pride*, 2007; *Rubino et al.*, 2009; *Solazzi et al.*, 2016] have been increasing during the last decades. WIFF is a frequency-dependent physical process that is mainly controlled by the permeability, the compressibility contrasts between the heterogeneities and the embedding background, and the geometrical characteristics of the heterogeneities. These properties are of significant relevance for flow and transport modeling, especially in fractured media [e.g. *Berkowitz*, 2002] and hence the analysis of the impact of WIFF on seismoelectric signals is of broad interest.

Despite its potential importance, only few studies have focused on the understanding of seismoelectric signals due to mesoscopic heterogeneities. In their pioneering numerical work, *Haartsen and Pride* [1997] mention a significant signal enhancement when considering a thin bed between two half-spaces, but no results or corresponding detailed physical explanations are presented. Similarly, *Haines and Pride* [2006] showed that layers that are up to 20 times thinner than the seismic wavelength could be detected by the seismoelectric method. More recently, *Grobbe and Slob* [2016] used numerical simulations to explore the enhancement of the interface response in the contact of two half-spaces when thin beds are located in between these half-spaces *(Cite Grobbe and Slob in this book)*. Although they study the constructive and destructive interferences resulting from different amounts and thicknesses of thin beds, they do not focus on the physical phenomena in the thin bed itself.

A likely explanation why mesoscopic effects on the seismoelectric signal have so far been largely ignored in the scientific literature is high computational cost of corresponding numerical simulations. This cost is due to the fact that the dominant scales at which WIFF takes place, as characterized by the corresponding diffusion lengths, are much smaller than the prevailing seismic wavelengths. Recently, *Jougnot et al.* [2013] presented a new approach for studying the seismoelectric response of mesoscopic heterogeneities that circumvents this limitation. Instead of performing numerical simulations of wave propagation, they simulated the seismoelectric response of oscillatory compressibility tests on synthetic samples at different frequencies. Since the size of the probed sample can be much smaller than the seismic wavelengths, this approach avoids the inherent problems related to the large contrasts in spatial scale between seismic wavelengths and diffusion lengths. The work by *Jougnot et al.* [2013] thus opens an avenue for detailed analyses of seismoelectric responses to mesoscopic heterogeneities. Here, we extend and complement this study. We first describe the underlying theoretical framework used to compute the seismoelectric response of an heterogeneous sample subjected to an oscillatory compressibility test. Next, we present an energy-based approach to characterize the seismoelectric response at the sample scale, as a substitute to relying on a certain experimental setup, such as, for example, a particular electrode configuration. In order to gain insights into the physical processes that contribute to the seismoelectric response in the presence of mesoscopic heterogeneities, we proceed to explore an analytical solution for a rock sample containing a horizontal layer centered in an otherwise homogeneous rock in an initial case and containing a fracture in a second analysis. We then perform a numerical sensitivity analysis of the seismoelectric signals generated in 2D fractured media. For different fracture properties, we present the spatial frequency dependence of the amplitude of the electrical potential signals as well as the frequency-dependent total energy converted to seismoelectric signal in an oscillation cycle.

2 Theory

To explore the seismoelectric signals produced by mesoscopic heterogeneities, we employ the methodology proposed by *Jougnot et al.* [2013]. We consider a 2D, fluid-saturated, heterogeneous porous rock sample and subject it to an oscillatory compression. The mechanical response of the probed sample is obtained by solving Biot's (1941) quasi-static equations in the space-frequency domain with adequate boundary conditions. The resulting fluid velocity field is then used to calculate the seismoelectric response of the sample. That is, we decouple the seismic and electrical problems [e.g., *Haines and Pride*, 2006; *Jardani et al.*, 2010; *Zyserman et al.*, 2010]. In the following, we present the details of the proposed methodology. It is important to mention here that the extension of this approach to 3D is conceptually straightforward, but computationally cumbersome.

2.1 Mechanical response

Let $\Omega = (0, L_x) \times (0, L_y)$ be a domain that represents the probed 2D sample and Γ its boundary given by

$$\Gamma = \Gamma^L \cup \Gamma^B \cup \Gamma^R \cup \Gamma^T, \tag{1}$$

where the subscripts L, R, B, and T stand for left, right, bottom, and top boundary, respectively,

$$\Gamma^L = \{(x,y) \in \Omega : \; x = 0\}, \tag{2}$$
$$\Gamma^R = \{(x,y) \in \Omega : \; x = L_x\}, \tag{3}$$
$$\Gamma^B = \{(x,y) \in \Omega : \; y = 0\}, \tag{4}$$
$$\Gamma^T = \{(x,y) \in \Omega : \; y = L_y\}. \tag{5}$$

We apply a time-harmonic normal compression at the top boundary of the sample. The solid is neither allowed to move on the bottom boundary nor to have horizontal displacements on the lateral boundaries. No tangential forces are applied on the lateral boundaries, and the pore fluid is not allowed to flow into or out of the sample. Thus, the following boundary conditions are imposed

$$\begin{aligned}
\boldsymbol{\tau}\cdot\boldsymbol{\nu} &= (0,-\Delta P)\,, \quad (x,y)\in\Gamma^T, &(6)\\
\boldsymbol{u} &= \mathbf{0}, \quad (x,y)\in\Gamma^B, &(7)\\
(\boldsymbol{\tau}\cdot\boldsymbol{\nu})\cdot\boldsymbol{\chi} &= 0, \quad (x,y)\in\Gamma^L\cup\Gamma^R, &(8)\\
\boldsymbol{u}\cdot\boldsymbol{\nu} &= 0, \quad (x,y)\in\Gamma^L\cup\Gamma^R, &(9)\\
\boldsymbol{w}\cdot\boldsymbol{\nu} &= 0, \quad (x,y)\in\Gamma, &(10)
\end{aligned}$$

where $\boldsymbol{\nu}$ denotes the unit outer normal on Γ and $\boldsymbol{\chi}$ is a unit tangent so that $\{\boldsymbol{\nu},\boldsymbol{\chi}\}$ is an orthonormal system on Γ. In addition, $\boldsymbol{\tau}$ is the total stress tensor, $\boldsymbol{u}$ is the average displacement of the solid phase, and $\boldsymbol{w}$ is the relative fluid-solid displacement.

As we are interested in quantifying WIFF effects on the seismoelectric signal, the response of the sample subjected to the oscillatory compressibility test is obtained by solving Biot's (1941) quasi-static equations. This approach is valid because the physical process is controlled by fluid-pressure diffusion and, thus, inertial effects can be neglected. In the space-frequency domain, these equations can be written as

$$\nabla\cdot\boldsymbol{\tau}=0, \tag{11}$$

$$i\omega\frac{\eta}{k}\boldsymbol{w}=-\nabla p_f, \tag{12}$$

where $i=\sqrt{-1}$ is the imaginary number, ω the angular frequency, p_f the fluid pressure, k the permeability, and η the fluid viscosity. Equation (11) represents the stress equilibrium within the sample, while Eq. (12) is Darcy's law. These two equations are coupled through the stress-strain relations

$$\boldsymbol{\tau}=\left(\lambda_u\nabla\cdot\boldsymbol{u}+\alpha_B M\nabla\cdot\boldsymbol{w}\right)\boldsymbol{I}+2G^{fr}\boldsymbol{\epsilon}, \tag{13}$$

$$p_f=-\alpha_B M\nabla\cdot\boldsymbol{u}-M\nabla\cdot\boldsymbol{w}. \tag{14}$$

In these equations, the involved coefficients are given by

$$M=\left[\frac{\alpha_B-\phi}{K^s}+\frac{\phi}{K^f}\right]^{-1}, \tag{15}$$

$$\alpha_B=1-\frac{K^{fr}}{K^s}, \tag{16}$$

$$\lambda_u=K^{fr}+M\alpha_B^2-\frac{2}{3}G^{fr}, \tag{17}$$

where K^{fr}, K^s, and K^f are the bulk moduli of the solid matrix, the solid grains, and the fluid phase, respectively, λ_u is the undrained Lamé constant, $\boldsymbol{\epsilon}$ is the strain tensor, ϕ is the porosity, and G^{fr} is the shear modulus of the bulk material, which is equal to that of the dry matrix.

The mechanical response of the sample subjected to the oscillatory compression is obtained by solving Eqs. (11) to (14) with the boundary conditions described by Eqs. (6) to (10). Since the methodology is based on Biot's (1941) quasi-static equations, it is limited to frequencies for which the resulting fluid flow is laminar. That is, the frequencies considered in the simulations should be smaller than Biot's (1962) critical frequency ω_c

$$\omega_c=2\pi f_c=\frac{\phi\eta}{k\rho^f}, \tag{18}$$

where ρ^f the density of the pore fluid.

In order to determine the spatial scales involved in the WIFF process in response to the applied oscillatory test, we consider a locally homogeneous medium. Without loss of generality, we explore the one-dimensional case for which the solid and relative fluid displacements,

u_y and w_y, occur in the vertical direction. Combining Eqs. (11) and (13) as well as Eqs. (12) and (14) leads to

$$\nabla^2 u_y = -\frac{\alpha_B M}{H_u} \nabla^2 w_y, \tag{19}$$

and

$$i\omega \frac{\eta}{k} w_y = \alpha_B M \nabla^2 u_y + M \nabla^2 w_y, \tag{20}$$

respectively. Next, substituting Eq. (19) into Eq. (20) results in

$$i\omega w_y = D \nabla^2 w_y. \tag{21}$$

Equation (21) is a diffusion equation with the diffusivity D given by

$$D = \frac{kN}{\eta}, \tag{22}$$

where $N = M - \alpha_B^2 M^2 / H_u$, H_u being the undrained plane-wave modulus. The spatial scale at which WIFF is significant is determined by the diffusion length

$$L_d \equiv \sqrt{D/\omega}. \tag{23}$$

2.2 Electrical response

The relative displacement between the pore fluid and the solid frame in response to the applied oscillatory compression results in a drag on the electrical excess charges of the EDL. This, in turn, generates a source or streaming current density $\boldsymbol{j_s}$. Since the distributions of both the excess charge and the microscopic relative velocity of the pore fluid are highly dependent on their distance to the mineral grains, not all the excess charge is dragged at the same velocity. Correspondingly, a moveable charge density $\underline{\hat{Q}}_V^0$ smaller than the total charge density $\underline{\bar{Q}}_V$ has to be considered [e.g., *Jougnot et al.*, 2012; *Revil and Mahardika*, 2013; *Revil et al.*, 2015; *Jougnot et al.*, 2015]. Note that, in the litterature, the moveable charge density may also be referred to as effective excess charge and written $\bar{Q}_v^{eff}$ [e.g. *Jougnot et al.*, 2012, 2015]. In the considered case, the source current density takes the form [e.g., *Jardani et al.*, 2010; *Jougnot et al.*, 2013]

$$\mathbf{J}^{i,e} = \underline{\hat{Q}}_V^0 i\omega \boldsymbol{w}, \tag{24}$$

where $i\omega\boldsymbol{w}$ is the relative fluid velocity. The moveable charge density formulation, which allows us to explicitly express the role played by the relative fluid velocity in the source current density generation, provides, for the same assumptions, equivalent results to the electrokinetic coupling coefficient formulation commonly used in the seismoelectric literature [e.g., *Pride*, 1994; *Jouniaux and Zyserman*, 2016]. The relationship between the moveable charge density and the electrokinetic coupling coefficient can be found in many works [e.g. *Revil and Leroy*, 2004; *Jougnot et al.*, 2012, 2015; *Revil and Mahardika*, 2013]. In the absence of an external current density, the electrical potential φ in response to a given source current density satisfies [*Sill*, 1983]

$$\nabla \cdot (\sigma^e \nabla \varphi) = \nabla \cdot \mathbf{J}^{\mathrm{i,e}}, \tag{25}$$

where σ^e denotes the electrical conductivity, which strongly depends on the saturating pore fluid as well as on textural properties of the medium, such as the porosity and the tortuosity [e.g. *Archie*, 1942; *Clennell*, 1997; *Revil and Linde*, 2006]. As we only consider low frequencies, that is, lower than Biot's critical frequency, we assume that displacement currents can be neglected.

In conclusion, we obtain the relative fluid-solid displacement field by solving Eqs. (11) to (14) under the boundary conditions corresponding to the applied test (Eqs. (6) to (10)). Next, this field is employed to determine the source current density field through Eq. (24). Finally, the electrical potential is obtained by solving Eq. (25) under pertinent boundary conditions.

2.3 Energy-based approach

The sensitivity of seismoelectric signals to parameters of interest, such as the background permeability or fracture properties, can be studied in different ways. Analytical expressions are helpful to build conceptual understanding based on idealized situations, while for more complex and realistic scenarios it is necessary to resort to numerical simulations. Typically, a particular experimental configuration is considered and differences in amplitude and spatial variations are studied [e.g., *Revil and Jardani*, 2009; *Jougnot et al.*, 2013; *Grobbe and Slob*, 2016]. From a theoretical point of view, it is interesting to consider an energy-based approach and study the total energy converted into seismoelectric signals. Although it would be impossible to quantify this parameter experimentally, it constitutes an attractive theoretical approach to obtain a global estimate of the sensitivity of the method that is independent of the specific experimental configuration.

The energy density of an electric field $\mathbf{E}(t)$ is given, in the space-time domain, by [e.g. *Feynman et al.*, 1965]

$$e(t) = \frac{1}{2}\varepsilon|\mathbf{E}(t)|^2, \tag{26}$$

where ε is the electric permittivity of the medium. Since displacement currents are negligible, the electric field at any time can be calculated as

$$\mathbf{E}(t) = \Re\left(\nabla(\varphi_0 e^{i\omega t})\right), \tag{27}$$

where φ_0 is the complex amplitude of the electrical potential derived for each frequency as explained in the previous section. The corresponding real part is taken because we solve the equations in the space-frequency domain.

Using average properties of time-harmonic complex-valued variables [*Rubino et al.*, 2006], it is straightforward to show that

$$< \Re\left(\nabla(\varphi_0 e^{i\omega t})\right)^{T_p} \Re\left(\nabla(\varphi_0 e^{i\omega t})\right) >= \frac{1}{2}\Re\left(\nabla\varphi_0^{T_p}\nabla\varphi_0^*\right), \tag{28}$$

where the operator $< . >$ denotes the average value over one oscillation cycle. Using Eqs. (27) and (28), we obtain

$$< |\mathbf{E}(t)|^2 >= \frac{1}{2}|\nabla\varphi_0|^2. \tag{29}$$

Using the expression for the energy density (Eq. (26)), we finally get

$$< \frac{1}{2}\varepsilon|\mathbf{E}(t)|^2 >= \frac{1}{4}\varepsilon|\nabla\varphi_0|^2 =< e(t) > . \tag{30}$$

Locally, the energy density converted into seismoelectric signal in one period of oscillation T_p can therefore be computed using

$$\int_o^{T_p} e(t)dt = \frac{1}{4}\varepsilon|\nabla\varphi_0|^2 T_p. \tag{31}$$

The total converted energy in the sample can then be calculated by integrating Eq. 31 over the spatial domain. Doing so for each frequency yields a spectrum of the total converted energy. This spectroscopic analysis makes it possible to determine a frequency at which this energy is maximum over the sample. In the following, we shall refer to this as the peak frequency.

2.4 Rock physical relationships considered in this study

Our focus is on the physics governing the generation of the seismoelectric signal in response to WIFF. For this reason, we only consider clean sandstones with different porosities of the matrix and idealized rock physical relationships to link material properties. To relate the porosity ϕ to the permeability k, we use the Kozeny-Carman equation [e.g., *Mavko et al.*, 2009]

$$k = b\frac{\phi^3}{(1-\phi)^2}d^2, \tag{32}$$

where b is a geometrical factor that depends on the tortuosity of the porous medium, and d the mean grain diameter. In this analysis, we take $b = 0.003$ [*Carcione and Picotti*, 2006] and $d = 8{\times}10^{-5}$ m [*Rubino et al.*, 2009]. These properties describe well-sorted fine-grained sandstone. In addition to changes in permeability, porosity variations also imply changes in the mechanical properties. To link the porosity and the solid grain properties with the elastic moduli of the dry frame, we use the empirical model of *Krief et al.* [1990]

$$K^{fr} = K^s (1-\phi)^{3/(1-\phi)}, \tag{33}$$

$$G^m = \frac{K^{fr}G^s}{K^s}, \tag{34}$$

where G^s is the shear modulus of the solid grains.

For the numerical study, we follow *Nakagawa and Schoenberg* [2007] and compute the elastic properties of the drained fracture in terms of the shear and drained normal compliances

$$\eta_T = \frac{h}{G_h^m}, \tag{35}$$

$$\eta_N = \frac{h}{K_h^{fr} + \frac{4}{3}G_h^m}, \tag{36}$$

where h is the fracture aperture and K_h^{fr} and G_h^m are its drained-frame bulk and shear moduli, respectively.

In this work, we consider only clean sandstones in which the surface conductivity can be neglected. Also, as we consider low frequencies, that is, frequencies lower than Biot's critical frequency, we can safely neglect EDL polarization effects and assume that the electrical conductivity has no imaginary part. Under this assumption, the electrical conductivity is given by

$$\sigma^e = \sigma^f \phi^{m^c} = \frac{\sigma^f}{F}, \tag{37}$$

where σ^f denotes the electrical conductivity of the pore water, while m^c and F are the cementation exponent and the formation factor as defined by *Archie* [1942], respectively. The pore water conductivity depends strongly on the amount of total dissolved salts [e.g. *Sen and Goode*, 1992].

The remaining electrical parameter $\underline{\hat{Q}}_V^0$ can be obtained by employing the empirical relationship proposed by *Jardani et al.* [2007]

$$\log\left(\underline{\hat{Q}}_V^0\right) = -9.2349 - 0.8219\log(k), \tag{38}$$

where k and $\underline{\hat{Q}}_V^0$ are in units of m^2 and C/m^3, respectively. Below Biot's critical frequency, the effective excess charge density is similar to the one at zero frequency [e.g., *Tardif et al.*, 2011; *Revil and Mahardika*, 2013] and, hence, boundary layer effects can be neglected in the test cases considered in the following. We use idealized rock physical relationships to link σ^e and $\underline{\hat{Q}}_V^0$ to porosity, but these properties can also be inferred independently by laboratory experiments [e.g., *Jouniaux and Pozzi*, 1995; *Suski et al.*, 2006]. Although $\underline{\hat{Q}}_V^0$ mainly depends on the permeability of the medium (Eq. 38), a recent study of *Jougnot et al.* [2015] highlighted that the pore water salinity also has a significant effect on its amplitude (around one order-of-magnitude change for a salinity change of four orders-of-magnitude).

The dielectric permittivity of the medium is usually expressed as the product of the dielectric permittivity of the vacuum ε_0 and the relative dielectric permittivity ε_r

$$\varepsilon = \varepsilon_r \varepsilon_0. \tag{39}$$

ε_r can be determined using a volume averaging approach [*Pride*, 1994; *Linde et al.*, 2006]

$$\varepsilon_r = \frac{1}{F} \left[\varepsilon_r^f + (F-1)\, \varepsilon_r^s \right], \tag{40}$$

where ε_r^f and ε_r^s are the relative permittivity of the water ($\varepsilon_r^f \simeq 81$) and the solid grains ($\varepsilon_r^s \simeq 5$), respectively. This model depends on the same parameter as the electrical conductivity, that is, the formation factor (Eq. 37), and thus, is directly related to the porosity ($F = \phi^{-m^c}$).

3 Insights from 1D analytical solutions

In some simple cases, the set of equations that govern the generation of seismoelectric signals due to WIFF can be solved analytically. Equations that explicitly relate the dependence of the resulting electrical potential on rock properties can be useful to understand the underlying physical processes. Recently, *Monachesi et al.* [2015] solved the governing equations presented in the previous section for a 1D case. Here, we present their main analytical solutions and results, based on which we then study the seismoelectric signal dependence on the background permeability and on the pore water salinity.

3.1 General solution for a thin layer

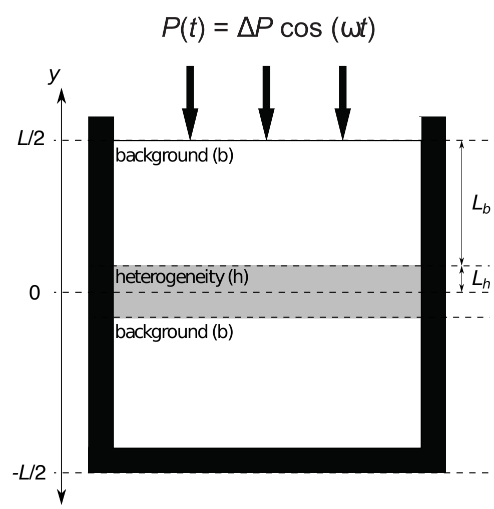

Figure 1. Schematic representation of the oscillatory compressibility test proposed by *Jougnot et al.* [2013] applied to a sample containing a single layer.

Monachesi et al. [2015] consider a thin layer of thickness $2L_h$ located at the center of an otherwise homogeneous rock sample (Fig. 1). In the following, properties related to the thin layer are identified by the subscript "h" for heterogeneity and the ones corresponding to the rest of sample by the subscript "b" for background. The thicknesses of the two embedding regions constituting the background are L_b and, thus, the total thickness of the sample is $2(L_h + L_b) = L$. Assuming a set of boundary conditions analogous to Eqs. (6) to (10), the boundary value problem given by Eqs. (11) to (14) can be solved in terms of the relative fluid-solid displacement $\boldsymbol{w}(y,\omega)$. Then, the current density $\boldsymbol{j_s}(y,\omega)$ can be computed from $\boldsymbol{w}(y,\omega)$ using Eq. (24). Finally, the electrical potential is obtained by solving Eq. (25) with the adequate boundary conditions. The resulting electrical potential as a function of the vertical position y and frequency ω is given by [*Monachesi et al.*, 2015]

$$\varphi(y,\omega) = \begin{cases} -\frac{i\omega \underline{\hat{Q}}_V^{0,h}}{\sigma_h^e}\frac{A_h}{\kappa_h}\left(e^{-\kappa_h|y|} + e^{\kappa_h|y|}\right) + S_h, & 0 \leq |y| \leq L_h, \\ -\frac{i\omega \underline{\hat{Q}}_V^{0,b}}{\sigma_b^e}\frac{A_b}{\kappa_b}\left(e^{-\kappa_b|y|} + e^{-\kappa_b(L-|y|)}\right) + S_b, & L_h \leq |y| \leq L/2, \end{cases} \tag{41}$$

where S_h, S_b, A_h, and A_b are given by

$$S_h = \frac{i\omega \underline{\hat{Q}}_V^{0,h}}{\sigma_h^e}\frac{A_h}{\kappa_h}\left(e^{-\kappa_h L_h} + e^{\kappa_h L_h}\right) - \frac{i\omega \underline{\hat{Q}}_V^{0,b}}{\sigma_b^e}\frac{A_b}{\kappa_b}\left(^{-\kappa_b L_h} + e^{-\kappa_b(L-L_h)} - 2e^{-\kappa_b L/2}\right), \tag{42}$$

$$S_b = \frac{2i\omega \underline{\hat{Q}}_V^{0,b}}{\sigma_b^e}\frac{A_b}{\kappa_b}e^{-\kappa_b L/2}, \tag{43}$$

$$A_h = \left(e^{-\kappa_h L_h} - e^{\kappa_h L_h}\right)^{-1} \frac{\Delta P\left(\beta_h - \beta_b\right)}{\sum_{j=h,b} N_j\kappa_j\ coth(\kappa_j L_j)}, \tag{44}$$

$$A_b = \left(e^{-\kappa_b L_h} - e^{-\kappa_b(L-L_h)}\right)^{-1} \frac{\Delta P\left(\beta_h - \beta_b\right)}{\sum_{j=h,b} N_j\kappa_j\ coth(\kappa_j L_j)}. \tag{45}$$

Note that the seismoelectric signal depends on the parameter k, which is related to the diffusion length, and, thus, among other parameters, to the permeability (see Eqs. 22 and 23) by

$$\kappa = \frac{\sqrt{i}}{L_d} = \sqrt{\frac{i\omega\eta}{kN}}, \tag{46}$$

and to the 1D Skempton coefficient β defined by

$$\beta \equiv \frac{\alpha_B M}{H_u}. \tag{47}$$

Equation (41), together with Eqs. (42) to (45), constitute the analytical solution of the seismoelectric response of a rock sample containing a central horizontal layer subjected to an oscillatory compressibility test as shown in Fig. 1. It is interesting to note that the seismoelectric response is highly dependent on both the medium permeability through $\underline{\hat{Q}}_V^{0,b}$ and κ, but also on the difference in the Skempton coefficients between the heterogeneity and the embedding background $\beta_h - \beta_b$, and thus on the compressibility contrast between heterogeneity and background. This finding is consistent with the literature on WIFF [e.g. *Müller et al.*, 2010].

To explore the dependence of the analytical solution on the various rock physical and structural parameters, we first consider a sample with a vertical side length of 20 cm composed of a stiff, low-permeability background with a porosity of 0.05 (Material 1 in Table 1), permeated at its center by a compliant, high-permeability horizontal layer with a thickness of 6 cm and a porosity of 0.4 (Material 2 in Table 1). The sample is subjected to a harmonic compression of amplitude ΔP=1 kPa at frequencies of 10^1, 10^2, and 10^3 Hz.

Figure 2a shows the amplitude profile of the resulting relative fluid velocity $dw/dt = i\omega w$ along the y-axis ($y \in [-L/2, L/2]$) for the three frequencies considered. Due to the strong contrast between the Skempton coefficients of the two materials, significant relative fluid velocities arise in both the background and the layer. The relative fluid velocity is higher near the contact between the layer and the background and vanishes at the center and at both edges of the sample. Under compression, the compliant layer compresses more than the material on either side of it with the result that water is forced out of the layer. The amplitude of dw/dt reaches larger values for higher frequencies. A significant current density j_s prevails in the background (Fig. 2b) due to the relative fluid velocity field (Fig. 2a) produced by the compression and the relatively large excess charge (Table 1). The maximum current densities occur at the contacts between the two materials, where the relative fluid velocity is also highest. Inside the layer, even though significant fluid flow also takes place, the resulting source

Table 1. Material properties employed in this work. Materials 1 and 2 are the same as the Materials 1 and 3 used by *Monachesi et al.* [2015], respectively.

Quartz grain bulk modulus K^s [GPa]	37		
Quartz grain shear modulus G^s [GPa]	44		
Water bulk modulus K^f [GPa]	2.25		
Water viscosity η [Pa $\times$ s]	0.001		
Water electrical conductivity σ^f[S m^{-1}]	0.01		
Water density ρ^f[Kg m^{-3}]	10^3		
	Material 1	Material 2	Material 3
Porosity ϕ	0.05	0.4	0.5
Dry rock bulk modulus K^{fr} [GPa]	31.47	2.88	0.017 / 0.04*
Dry rock shear modulus G^{fr} [GPa]	37.42	3.42	0.01 / 0.02*
Permeability k [mD]	2.66	3410	9600
Electrical conductivity σ^e [S m^{-1}]	2.5×10^{-5}	1.6×10^{-3}	2.5×10^{-3}
Moveable charge density $\underline{\hat{Q}}_V^0$ [C m^{-3}]	526.8	1.49	0.637
Biot's critical frequency f_c [Hz]	2.99×10^6	1.8×10^4	8.29×10^3

* Calculated using Eqs. (35) and (36) for apertures of 0.03 / 0.06 cm, respectively.

current density is small since the effective excess charge is much smaller in this material characterized by a larger permeability (Table 1, Eq. 38).

Significant electrical potential amplitudes (Fig. 2c), well above the $\simeq 0.01$ mV detectability threshold of laboratory experiments (e.g. *Zhu and Toksöz* [2005]; *Schakel et al.* [2012]), arise in response to the oscillatory compression. These results are consistent with those by *Jougnot et al.* [2013] for fractured rocks and point to the importance of WIFF effects on seismoelectric signals in the presence of porosity variations. Inside the layer, the amplitude of the electrical potential is constant. This is due to the negligible source current density in this high-permeability material. Because the electrical potential is continuous, this corresponds to the value of the electrical potential at the contact between the two materials.

The resulting electrical potential is not only characterized by its amplitude but also by its phase θ. In the background, θ shows rapid spatial changes when the frequency is high (Fig. 2d). Inside the layer, θ remains constant, which is in agreement with the behavior observed for the amplitude of the electrical potential in this region (Fig. 2c). In general, the phase values vary strongly within the medium and cover a much larger range than could be expected from a frequency-dependent electrical conductivity. For example, *Kruschwitz et al.* [2010] report a typical induced polarization phase of less than 0.6° for a large frequency range ($f \in$[10^{-3}; 10^4] Hz), while our calculations show a distribution -180 to +180° (Fig. 2d). This confirms that our assumption concerning the negligible effect of complex conductivity at low frequencies is valid (see section 2.4).

The behavior of the electrical potential curves as a function of normalized time is shown in Fig. 3 for the three frequencies considered. The curves correspond to the electrical potential differences $\Delta\varphi$ recorded by an electrode located at the center ($y = 0$) and a reference electrode located at one edge of the sample ($y = L/2$ or $y = -L/2$). Note that the integer values of t/T_p correspond to the moment of maximum applied stress. This representation allows us to interpret the physical mechanisms in a simple manner: during the compression cycle of the applied normal stress, the fluid inside the compliant layer experiences a pressure increase and thus water flows from the layer into the background, generating a significant seismoelectric signal. Conversely, during the extension cycle, water flows from the background

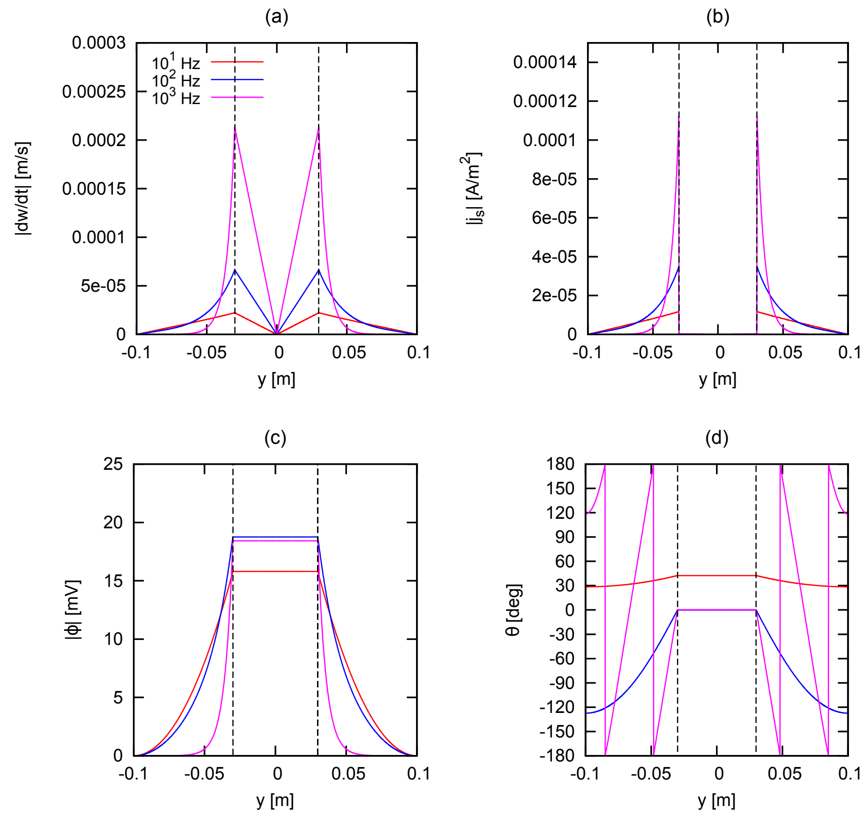

Figure 2. (a) Amplitude of relative fluid velocity dw/dt, (b) amplitude of electrical source current density j_s, and (c) amplitude $|\varphi|$ and (d) phase θ of the electrical potential corresponding to a rectangular, stiff, low-permeability background containing a compliant, high-permeability horizontal layer at its center. The porosity of the layer is 0.4 (Material 2 in Table 1), whereas that of the background is 0.05 (Material 1 in Table 1). In all cases, the panels show the parameters as functions of y. For visualization purposes, we denote the boundaries of the layer by dashed lines.

into the layer, generating a seismoelectric signal with an opposite sign. Note that the amplitude and phase of the electrical potential at 10^2 and 10^3 Hz are similar with a negligible phase lag with respect to the applied pressure. In contrast, the 10 Hz signal depicts different amplitude and phase values. These differences in amplitude and phase are also evident in Figs. 2c and d.

In order to explore in detail the dependence of the electrical potential on the frequency of the oscillatory compression, we show in Fig. 4a the amplitude of the electrical potential along the y-axis of the sample for frequencies between 1 Hz and 10^4 Hz [see *Monachesi et al.*, 2015, for the spatial-frequency dependence of the phase]. Between ∼10 and ∼100 Hz, the spatial extent and amplitude of the electrical potential in both the background and the layer are larger than for other frequencies. It is not straightforward to assign a frequency of maximum spatial extent since different amplitude iso-values have different corresponding frequencies of maximum spatial extent. At low frequencies (1-10 Hz), the electrical potential tends to become negligible. At higher frequencies (100-10000 Hz), WIFF is comprised in the immediate vicinity of the boundaries of the layer and the magnitude of the electrical potential is non-zero only inside the layer. In agreement with Figs. 2c and d, the amplitude of the electrical potential remains constant inside the layer at each frequency.

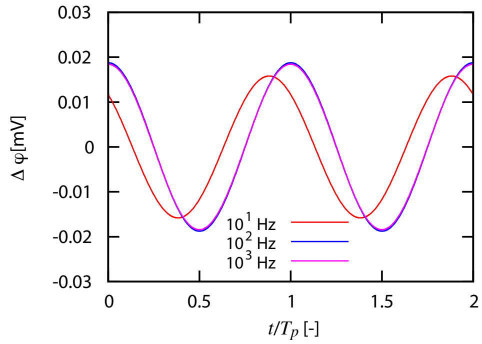

Figure 3. Electrical potential differences $\Delta\varphi$ between an electrode located at the center of the sample and a reference electrode located at an edge of the sample as functions of the normalized time t/T_p for frequencies of 10^1, 10^2, and 10^3 Hz.

In Figure 4b we show the distribution of the electrical potential amplitude obtained when the material properties of the background and the layer are interchanged. Due to the imposed boundary conditions, when the layer is stiffer and less permeable than the background, the electrical potential has a significant amplitude only inside the layer. The electrical potential amplitude is also frequency-dependent, with a maximum at the center of the layer and for a frequency that is higher compared to the previous situation [*Monachesi et al.*, 2015].

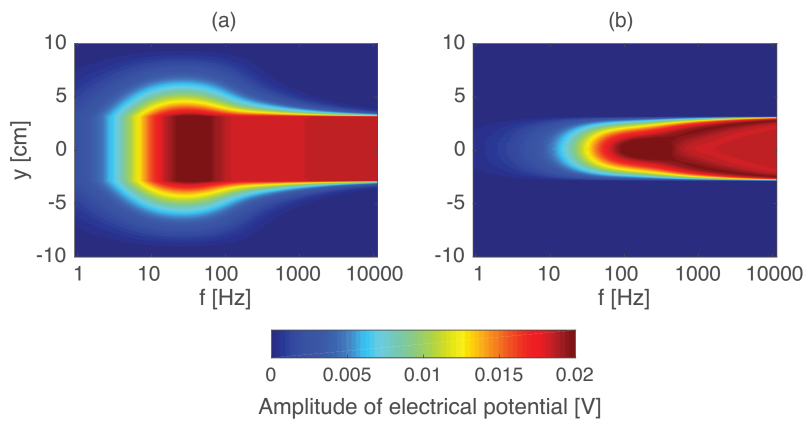

Figure 4. Amplitude of the electrical potential along the y-axis as a function of frequency corresponding to (a) a stiff, low-permeability background containing a compliant, high-permeability horizontal layer at its center, and (b) a compliant, high-permeability background containing a stiff, low-permeability horizontal layer at its center. Adapted from *Monachesi et al.* [2015].

3.2 Particular solution for a single fracture

Monachesi et al. [2015] also studied the seismoelectric signal of an homogeneous rock sample that is permeated by a single horizontal fracture. This was done by adapting their analytical solution to an infinitely thin layer at the center of the sample. This yields a simpler expression of the seismoelectric response

$$\varphi(y,\omega) = -\frac{i\omega \underline{\hat{Q}}_V^{0,b}}{\sigma_b^e} \frac{\bar{A}_b}{\kappa_b} \left(e^{-\kappa_b |y|} + e^{-\kappa_b (L-|y|)} - 2e^{-\kappa_b (L/2)} \right), \tag{48}$$

where

$$\bar{A}_b = \lim_{L_h \to 0} A_b = \frac{\Delta P \left(1 - \beta_b\right)}{\frac{b}{Z_N}\left(1 - e^{-\kappa_b L}\right) + N_b \kappa_b \left(1 + e^{-\kappa_b L}\right)}, \tag{49}$$

and Z_N is the drained normal compliance of the fracture. Note that Z_N is the only fracture parameter in these equations, while the only structural parameter is the total thickness of the sample L. It is also interesting that the seismoelectric signal mainly depends on the background permeability k_b through κ_b (Eq. 46) and $\underline{\hat{Q}}_V^{0,b}$ and on the background Skempton coefficient β_b. Figure 5a shows the spectroscopic analysis for a sample with the same size and background material as in Fig. 4a (Material 1 in Table 1) permeated by a fracture. Note the high amplitudes reached in this case due to the strong compressibility of the fracture.

3.3 Sensitivity to the background permeability

From the presented analytical solutions, it is clear that the background permeability has a predominant role in the generation of seismoelectric signals. Figure 5b shows the resulting seismoelectric signal when the background permeability is one order-of-magnitude larger than in Material 1, that is, k_b =26.6 mD. As opposed to what was presented by *Monachesi et al.* [2015], we let the permeability vary independently of the porosity, which does not change, so that the changes observed are uniquely related to permeability changes. We can observe two different effects: as the permeability increases, the maximum amplitude of the signal increases and the frequency of maximum extent of the signal is shifted towards higher frequencies. This result is consistent with the ones discussed by *Jougnot et al.* [2013]. The spatial scale at which WIFF occurs depends on the diffusion length and, therefore, on the background permeability (Eq. 46). Therefore, the frequency of maximum extent of the signal is mainly controlled by the background hydraulic properties, which is consistent with the asymptotic analysis by *Monachesi et al.* [2015]. The shift of maximum WIFF to higher frequencies related to a larger permeability also implies a higher fluid velocity and thus a higher amplitude of the electrical potential (Fig. 2). The amplitude of the seismoelectric signal is also affected by the imposed relationship between the moveable charge density and the background permeability (Eq. 38). A larger permeability implies a smaller moveable charge density and thus a decrease of the amplitude. The significant increase in amplitude shown in Fig. 5b suggests that the effect of a larger fluid velocity due to the shift to higher frequencies dominates over the amplitude decrease due to the smaller moveable charge density.

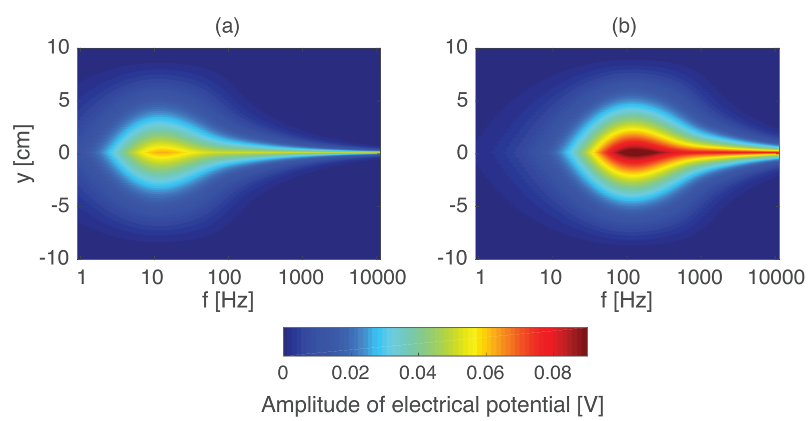

Figure 5. Seismoelectric response of a sample containing a fracture at its center (Eqs. 48 and 49) and its dependence on the background permeability. Amplitude of the electrical potential along the y-axis as a function of frequency (a) for the background properties corresponding to Material 1 (Table 1, k_b = 2.66 mD) and (b) for a background permeability that is one order-of-magnitude larger (k_b = 26.6 mD). Adapted from *Monachesi et al.* [2015].

3.4 Sensitivity to the pore water conductivity

The moveable charge density is not only influenced by the permeability. As discussed by *Jougnot et al.* [2015], the pore water salinity, and thus the pore water electrical conductivity σ^f, also affects their moveable charge density through its influence on the thickness of the EDL and the associated changes of the Zeta potential [e.g. *Revil et al.*, 1999]. In addition, the pore water conductivity also strongly affects the bulk electrical conductivity (Eq. 37). To study the effect of salinity changes on the seismoelectric signal, we complemented our spectroscopy analysis for a pore water conductivity that is one order-of-magnitude smaller (σ^f = 0.001 S m^{-1}, Fig. 6a) and one order-of-magnitude larger (σ^f = 0.1 S m^{-1}, Fig. 6b) than in the previous cases (σ^f = 0.01 Sm^{-1}, Fig. 5a). We calculated the corresponding moveable charge density as deviations from the value given by Eq. 38 with the model proposed by *Jougnot et al.* [2015]. This results in values of $\underline{\hat{Q}}_V^{0,b}$ = 790.12 C m^{-3} and 351.31 C m^{-3}, for σ^f = 0.001 S m^{-1}, and σ^f = 0.1 S m^{-1}, respectively. Not surprisingly, the impact of salinity/pore water conductivity upon the seismoelectric signal is significant: the lower the pore water conductivity, the higher the amplitude of the signal. The frequency of maximum extent of the signal is not affected by a change in pore water conductivity. Note here that the influence of fluid conductivity on the seismoelectric response is more important due to its effect on the bulk electrical conductivity (Eq. 37) than to its impact on $\underline{\hat{Q}}_V^{0,b}$, which can be considered a secondary effect [*Jougnot et al.*, 2015].

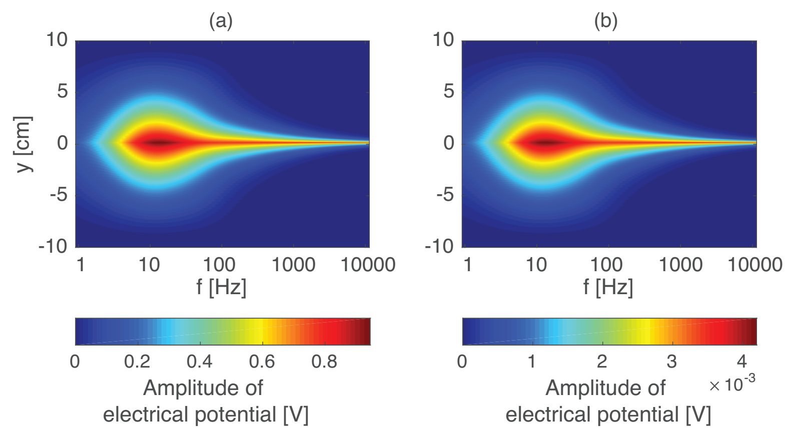

Figure 6. Seismoelectric dependence on pore water electrical conductivity. Amplitude of the electrical potential along the y-axis as a function of frequency for the same sample as shown in Fig. 5a but considering a pore water salinity that is (a) one order-of-magnitude smaller (σ^f = 0.001 S m^{-1}) and (b) one order-of-magnitude larger (σ^f = 0.1 S m^{-1}). Given the large amplitude difference, we use separate color scales for each subplot.

4 Numerical study of fractured rock samples

In this section, we numerically solve the governing equations described in the theory section in order to consider 2D fracture geometries. We employ the numerical strategy presented by *Jougnot et al.* [2013] for exploring the generation of seismoelectric signals due to WIFF in the presence of fractures. That is, we consider a 2D synthetic rock sample containing mesoscopic heterogeneities. Equations (11) to (14) are solved, with the boundary conditions described by Eqs. (6) to (10), using a finite element procedure [*Rubino et al.*, 2009]. From the resulting 2D velocity fields, we compute the electrical current density (Eq. 24) and then numerically solve Eq. (25) assuming perfect electrical insulation along the boundaries using a finite volume approach. To do so, we adapted an open source finite volume numerical code that was originally conceived to solve subsurface fluid flow problems [*Künze et al.*, 2014] to the considered electrical problem. In an initial analysis, we consider a synthetic homogeneous rock sample containing a simple 2D fracture. We then study the effects of different fracture lengths, different fracture orientations, and different numbers of fractures in the sample. Finally, fracture networks with varying degrees of connectivity are explored.

4.1 Analysis for a single fracture

We first consider a simple case corresponding to a homogeneous rock containing a horizontal fracture at its center (Fig. 7a). For the background material, we use for all cases the same sandstone as in the analytical study (Material 1 in Table 1). The fracture is modeled as a very compliant poroelastic rectangle that is characterized by large values of porosity and permeability (Material 3 in Table 1), with the elastic properties being calculated using Eqs. (35) and (36). Given that the fracture does not permeate the entire sample, the analytical solution presented in the previous section cannot be used and, instead, the numerical approach is employed. This initial case will be the basic geometry for which we will perform the 2D sensitivity analysis.

We consider a sample of 6×6 cm^2 with a horizontal fracture of 3 cm length and 0.03 cm aperture located at its center (Fig. 7a). We use 600×600 elements to discretize the entire domain. The numerical simulations using this mesh were compared to simulations using finer meshes to ensure the accuracy of the calculations. We compute the seismoelectric response of oscillatory compressions with $\Delta P = 1$ kPa at 40 different frequencies equally spaced on a logarithmic scale between 1 and 10,000 Hz.

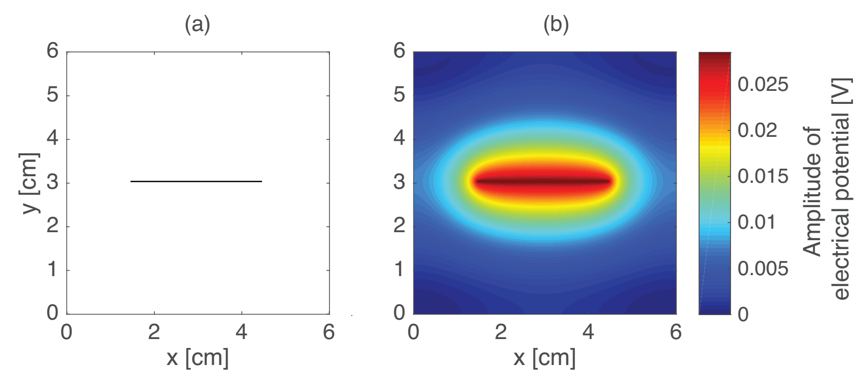

Figure 7. (a) Synthetic rock sample used as the basis to study the seismoelectric dependence on the properties of fractured media. A single horizontal fracture is embedded in an otherwise homogeneous medium. The sensitivity analysis presented in the following is based on simple variations of this initial model. (b) Amplitude of the electrical potential generated for a frequency of 142 Hz with a virtual reference electrode located at the left bottom edge of the sample. The amplitude of the stress applied on the top boundary of the sample ΔP is 1 kPa.

Figure 7b shows the resulting seismoelectric signal amplitude for a frequency of 142 Hz. Note that the electrical problem has been solved using a reference electrode at the origin (x = 0 cm, y = 0 cm). The electrical potential generated by this small heterogeneity is maximal in the immediate vicinity of the fracture and easily measurable with typical experimental set-up in the laboratory. This large signal is due to the high compressibility contrast between the fracture and the background, which in turn results in significant WIFF.

In Fig. 7, we display the detailed spatial distribution of the electrical potential for a single frequency in order to stress the 2D nature of the signal. However, the main interest of our approach is to study the spectral dependence of the signal generated by the oscillatory compression through a spectroscopic analysis. In order to best represent these results, Figure 8a shows vertical cuts of the seismoelectric signal amplitude through the center of the sample shown in Fig. 7a (x = 3 cm) as a function of frequency. These vertical cuts, which pass through the center of the fracture, are similar to those presented in the analytical section, but it should be noted that samples are 2D. To complete our study, we use the results of the energy-based analysis that we developed in Section 2.3 to provide a global measure of the frequency dependence of the seismoelectric signal in the sample. Figure 8b shows the total energy converted to the seismoelectric signal in one compression cycle as a function of frequency. To calculate this value, we numerically computed for each frequency the gradient of the electrical potential amplitude (Eq. 31) and summed the squared contribution of each pixel weighted by its electrical permittivity (Eqs. (39) and (40)) multiplied by one fourth of the corresponding period. The resulting spectrum shows a strong dependence of the converted electric energy on frequency and a clearly defined peak frequency for which the converted electric energy is maximum. In this case, the peak frequency corresponds to 142 Hz, which is the frequency used for the 2D representation in Fig. 7b.

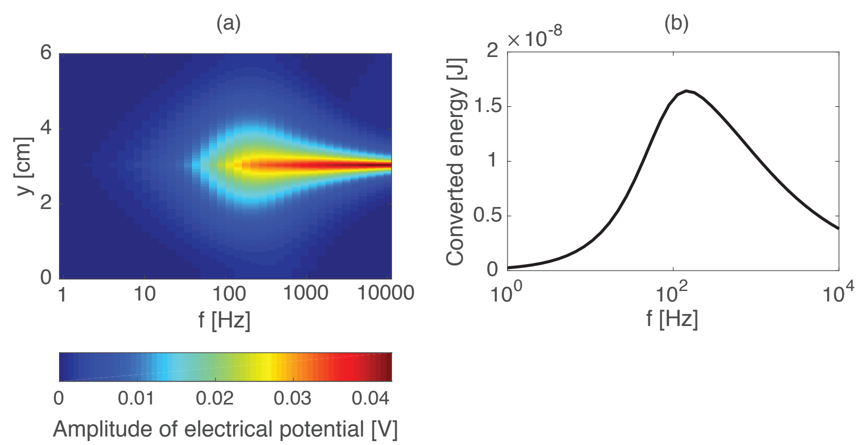

Figure 8. Vertical cuts of the electrical potential at the center (x = 3 cm) of the sample shown in Fig. 7a as a function of frequency. (a) Amplitude and (b) total energy converted to seismoelectric signal in one cycle as a function of frequency.

4.2 Sensitivity to the fracture extent

In this subsection, we investigate the effect of the fracture extent along the x-axis in the sample on the amplitude of the seismoelectric signal. We consider two cases where the fracture extent is smaller than in the previous section, with fracture lengths of 0.6 and 1.8 cm (Figs. 9a and c, respectively), and two cases where the extent is larger, that is, 4.2 and 6 cm (Figs. 9e and g, respectively). The latter corresponds to the extreme case of a fracture that permeates the whole sample. As the fracture length increases, so does the spectral range at which the fracture can be detected, the amplitude of the signal, and the vertical extent of the measurable electrical potential (Figs. 9b, e, h, and k). From the converted energy (Figs. 9c, f, i, and l) we can also see that the fracture extent changes the peak frequency at which the converted energy is higher; larger fractures imply a lower peak frequency and a higher amount of converted energy. Note that a one order-of-magnitude change in the fracture length from the sample in Fig. 9a to the one in Fig. 9j implies a shift of almost two orders-of-magnitude in the peak frequency and an increase of more than two orders-of-magnitude in the converted energy.

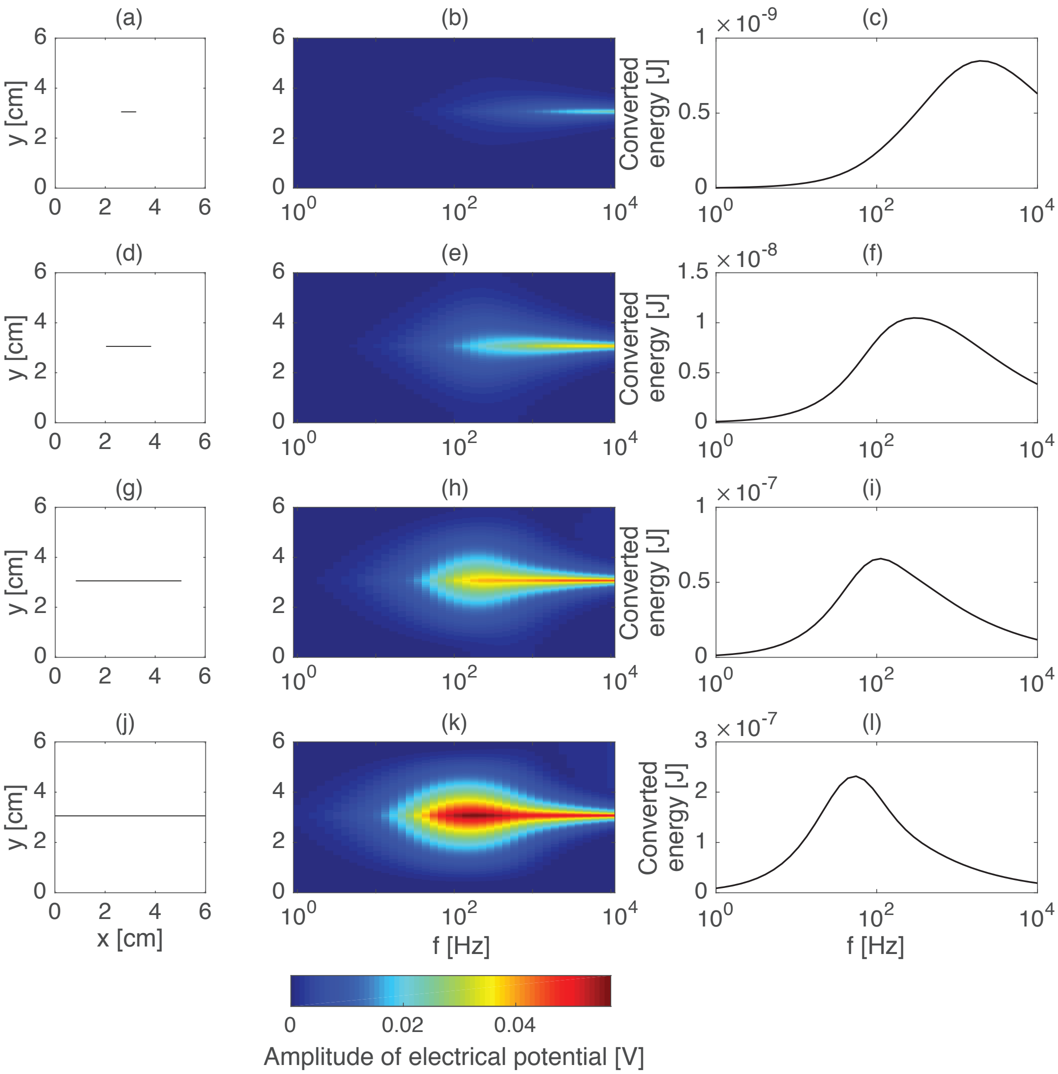

Figure 9. Dependence of seismoelectric signals on fracture length. (a), (d), (g) and (j) Samples with the same properties as Fig.7a but with different fracture lengths. (b), (e), (h) and (k) Vertical cuts of the amplitude of the electrical potential at the center (x = 3 cm) of the corresponding samples as functions of frequency. (c), (f), (i) and (l) Total converted electrical energy as a function of frequency.

4.3 Sensitivity to the fracture orientation

To understand the sensitivity to the fracture orientation, we consider four cases where a 3 cm long fracture is oriented from sub-horizontal to vertical with respect to the x-axis (see Figs. 10a, d, g, j and the figure caption for the fracture angles). As the orientation of the fracture becomes more vertical, the amplitude of the electrical potential decreases. WIFF takes place from the more compliant fracture to the stiff background and vice versa, and is maximum when the fracture is perpendicular to the direction of applied stress. In the latter case, the applied stress strongly deforms the fracture, increases its fluid pressure and produce significant WIFF and seismoelectric conversion. Conversely, in the extreme case of a vertical fracture, the fluid mainly flows inside the fracture, which has a low $\underline{\hat{Q}}_V^{0,h}$ and therefore does not produce a significant electrical source current density. The intermediate states (Figs. 10a, d, and g) show the smooth transition between a horizontal to a vertical fracture. The orientation does not affect the peak frequency, although the total converted energy is, as expected, significantly smaller for more vertically oriented fractures (Figs. 10 c, f, i and l).

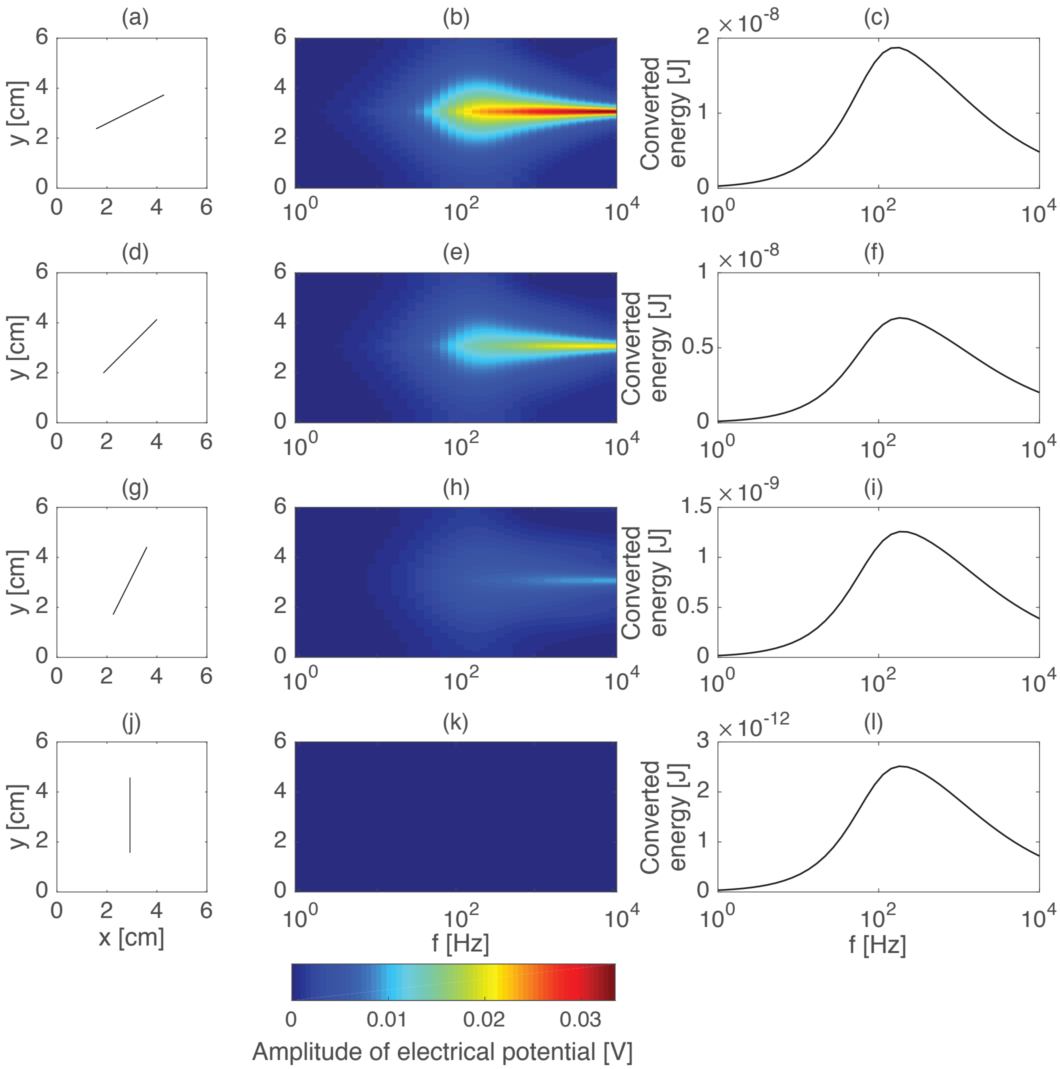

Figure 10. Dependence of seismoelectric signal on fracture orientation. (a), (d), (g) and (j) Samples with the same properties as Fig. 7a but with different fracture orientation, ranging from sub-horizontal to vertical. The angles with respect to the x-axis are: (a) 27°, (d) 45° , (g) 67.5° and (j) 90°. (b), (e), (h) and (k) Vertical cuts of the amplitude of the electrical potential at the center (x = 3 cm) of the corresponding samples as functions of frequency. (c), (f), (i) and (l) Total converted electrical energy as a function of frequency.

4.4 Sensitivity to the number of fractures

To understand the aggregate effect of multiple fractures, we consider an increasing amount of fractures in a sample of the same size as in the previous cases. The starting point is a single fracture as shown in the fracture extent subsection (Fig. 9j). We then consider cases with 2, 3, 4 and 5 equally spaced fractures throughout the sample (Figs. 11 a, d, g, and j). The corresponding fracture spacings are 2.97, 1.97, 1.47, and 1.17 cm, respectively. Regardless of the number of fractures in the sample, the maximum amplitude of electrical potential does not significantly change. As the number of fractures in the sample increases, the vertical extent of the seismoelectric signal generated by each fracture decreases and the spectral range where the signal could be detected is shifted towards higher frequencies. Correspondingly, the energy plots in Fig. 11 show that the peak frequency for which the maximum of energy is converted also shifts to higher values as the number of fracture increases. This shift in frequency corresponds to the dependence of the diffusion length (Eq. 23) on the frequency; by decreasing the space between fractures, we decrease the spatial scale at which WIFF between the fractures can take place, thus the frequency corresponding to the maximum extent of fluid flow is higher. It is interesting to note that although the peak frequency is affected by the number of fractures in the sample, this parameter does not seem to influence the total converted energy at the corresponding peak frequency (Fig. 11). This suggests that the larger number of fractures compensates for the smaller spatial extent of the region in which significant electrical potential amplitude are produced by each fracture in the sample.

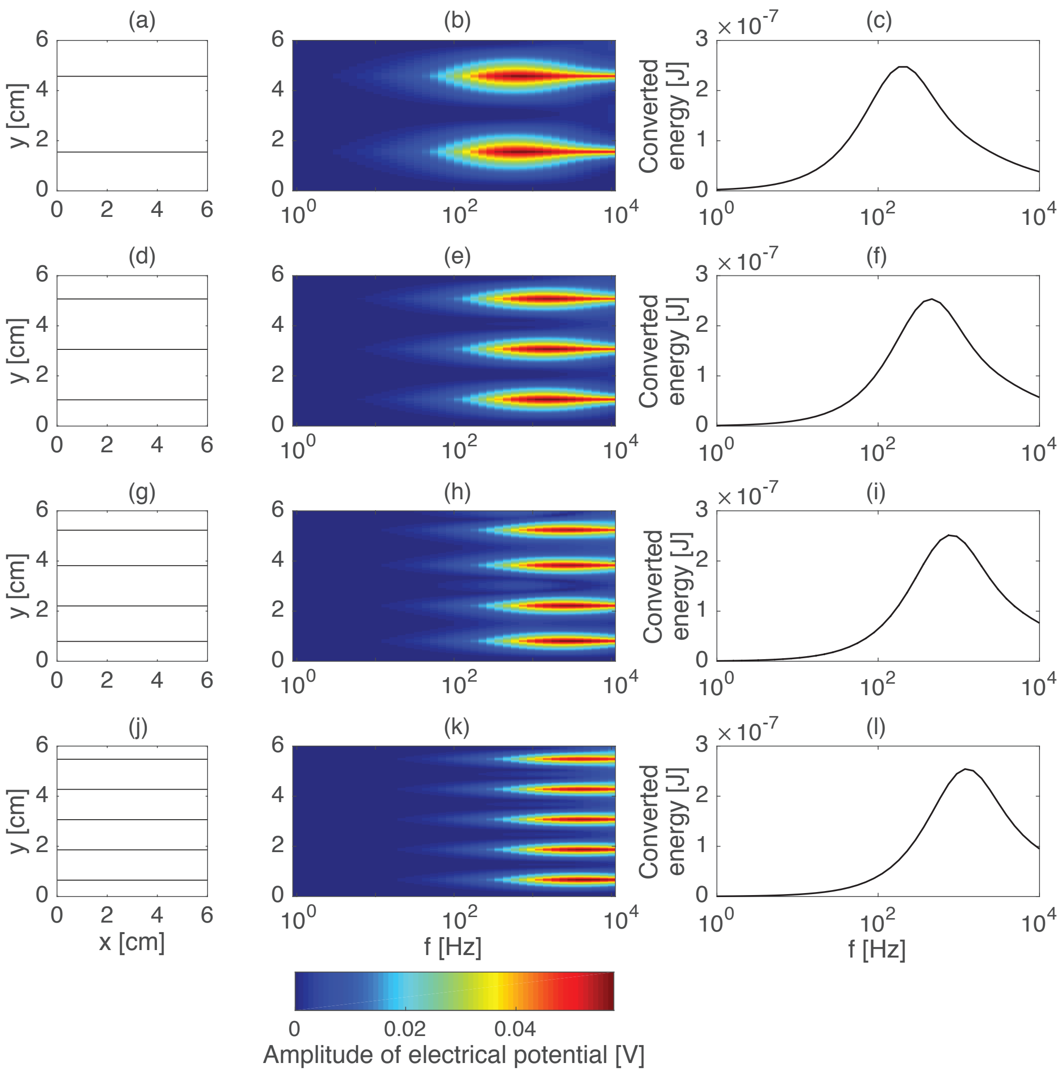

Figure 11. Dependence of seismoelectric signal on fracture density. (a), (d), (g) and (j) Samples with the same properties as Fig.7a but with different number of fractures. (b), (e), (h) and (k) Vertical cuts of the amplitude of the electrical potential at the center (x = 3 cm) of the corresponding samples as functions of frequency.

4.5 Analysis of a fracture network

In this subsection, we study the effects of fracture connectivity on the seismoelectric signal. We consider a similar setup as the one used by *Rubino et al.* [2014] to explore the dependence of the seismic attenuation on fracture connectivity. We consider a sample of 20×20 cm^2, discretized by $1000{\times}1000$ elements, and examine four different fracture scenarios. In the first scenario, horizontal fractures are randomly distributed in the sample (Fig. 12a). In the second scenario, the horizontal fractures are retained and vertical fractures are added randomly under the constraint that none of the fractures is connected to another one (Fig. 12c). The third case corresponds to the same number of horizontal and vertical fractures, but with some of the vertical fractures being connected to the horizontal ones (Fig. 12e). Finally, in the fourth scenario we consider the case when all the vertical fractures are connected to some of the horizontal ones (Fig. 12g). In all the examples, the fractures have an aperture of 0.06 cm. The fracture properties are given in Table 1 (Material 3). The maximum pressure applied is the same as in all other examples, that is, $\Delta P =$1 kPa, and all the boundary conditions remain the same as in previous cases.

Figure 12 shows the amplitude of the electrical potential of the four geometries considered for a frequency of 0.73 Hz. We observe that the presence of vertical fractures that are not connected to the horizontal ones does not significantly change the amplitude of the seismoelectric response (Figs. 12b and e). However, when the vertical fractures are connected to the horizontal ones, the spatial distribution and amplitude of the electrical potential does change (Figs. 12h and k). Indeed, the maximum amplitude in the sample is lower for a higher fracture connectivity and larger parts of the sample are "illuminated" with a measurable electrical potential in this case.

To study the dependence of the seismoelectric signal on fracture connectivity at the sample scale, we present in Fig. 13 plots of the total converted electrical energy. A clear dependence on fracture connectivity can be observed. Adding the unconnected vertical fractures results in a higher seismoelectric energy, but as the fracture connectivity increases, there is a decrease in the total energy of the electric field. The peak frequency is also affected by the degree of connectivity. When the vertical unconnected fractures are added, the peak frequency does not change and corresponds to 0.73 Hz, which was the frequency used in Fig. 12. Increasing the fracture connectivity shifts the peak frequency to higher values.

5 Discussion and conclusions

Following *Jougnot et al.* [2013] and *Monachesi et al.* [2015], we performed a theoretical (analytical and numerical) study of the seismoelectric signals generated when a rock sample containing mesoscopic heterogeneities is submitted to an oscillatory compressibility test. Heterogeneities are considered mesoscopic when their size is smaller than the typical wavelength but larger than the pore-scale. In the present contribution we focused on mesoscopic fractured media and developed a quantitative approach to characterize the dependence of the seimoelectric signal with fracture connectivity. The predicted signal is highly frequency-dependent and hence we illustrated our results in terms of the space-frequency distribution of the seismoelectric response, which corresponds to a spectroscopic analysis. The source of this frequency-dependent signal is linked to WIFF from the more compliant heterogeneities to the background during the compression cycle, and in the opposite direction during the dilatation cycle. Our results show that this phenomenon yields measurable seismoelectric signals under typical laboratory set-ups in terms of applied pressure, frequency range, and instrument resolution [e.g. *Batzle et al.*, 2006; *Subramaniyan et al.*, 2014; *Pimienta et al.*, 2015]. The use of the energy-based approach presented in Section 2.3 provides complementary information to our spectroscopic analysis at the sample scale by allowing for the definition of a peak frequency for which the total converted seismoelectric energy is maximum.

We studied different kinds of mesoscopic heterogeneities: thin layers, single fractures and fracture networks. Our results show a strong dependence of the seismoelectric signal on mechanical, hydraulic, and structural properties of the background and the mesoscopic heterogeneities. In particular, the background permeability via the diffusion length, fracture separation and fracture length, control the frequency at which maximum WIFF occurs and, therefore, also influences the peak frequency. The amplitude of the electrical potential is mainly controlled by the background permeability, the pore water conductivity, compressibility contrast between heterogeneity and background, and fracture orientation. These parameters affect the bulk conductivity, moveable charge density, and source current density, which define the electrical potential distribution in the sample. Similar to what was observed by *Rubino et al.* [2013, 2014] for the seismic case, fracture orientation, extent, density, and connectivity influence the spectroscopic signature of the seismoelectric signal. This is particularly interesting for the characterization of fractured media, which is of primary importance in hydrological applications yet extremely difficult to achieve in practice [e.g. *Berkowitz*, 2002].

Connected fractures reduce the total energy converted to the seismoelectric signal and change the spatial distribution of electrical potential amplitude. For an equal number of vertical fractures, the total converted electrical energy decreases by $\sim$50% for the corresponding peak frequency (Fig. 13) when these fractures are connected with horizontal ones. The reason for this is that the connection to vertical fractures enables part of the fluid pressure increase in response to the applied stress to be released from the horizontal fractures into these highly permeable regions. This reduces the fluid pressure gradient and, thus, the fluid flow between fractures and background, which in turn results in a decrease of the generated electrical source current density and the measurable electrical potential outside the fractures. Given that the degree of fracture connectivity controls the effective hydraulic properties of fractured rocks, this connectivity effects are potentially important as they may help to extract this kind of information from corresponding seismoelectric measurements.

The present contribution describes analytical and numerical experiments and aims at understanding how mesoscopic heterogeneities can produce measurable seismoelectric signals under laboratory conditions. To the best of the author's knowledge, these prediction have not yet been tested in practice. Such experimental studies would be of significant interest for both the rock physics and the seismoelectric community as they may provide a new rock physical characterization tool: seismoelectric spectroscopy.

Besides thin layers or fractures, other types of mesoscopic heterogeneities are known to generate significant WIFF [e.g. *Batzle et al.*, 2006; *Adam et al.*, 2009; *Müller et al.*, 2010; *Pimienta et al.*, 2015] but remain unexplored in terms of their seismoelectric response. Similar effects also exist in patch-type partially saturated conditions [e.g. *Caspari et al.*, 2011; *Masson and Pride*, 2011; *Rubino and Holliger*, 2012]. Such saturation effects and the resulting seismoelectric signals could explain some discrepancies between experimental data and current models, such as those shown by *Bordes et al.* [2015].

The results of this study could also help to better understand seismoelectric conversions at the field scale. Indeed, all geological formations contain a certain degree of mesoscopic heterogeneity and, therefore, seismic waves are expected to produce seismoelectric signals associated with such heterogeneities as they propagate. These phenomena could be one of the causes for the difficulties encountered in seismoelectric field applications. For example, high noise levels encountered in field applications [e.g. *Strahser et al.*, 2011] could be related to heterogeneities of different nature and size that generate multiple seismoelectric source currents when traversed by the seismic waves. Further studies accounting for effects such as geometrical divergence and the co-seismic field will be carried in the near future to fully understand the relative contribution of Biot's slow waves to the total seismoelectric signal that would be measured in the field. Our results clearly illustrate that a better understanding of the role played by mesoscopic heterogeneities is essential for the development of the seismoelectric method.

Acknowledgments

This work was partly financed by the Swiss National Science Foundation. This is IPGP contribution number xxxx.

References

Adam, L., M. Batzle, K. Lewallen, and K. van Wijk (2009), Seismic wave attenuation in carbonates, *J. Geophys. Res.*, *114*(B6), 6208.

Archie, G. (1942), The electrical resistivity log as an aid in determining some reservoir characteristics, *Trans. Ame. Inst. of Min. and Metall. Eng.*, *146*, 54–61.

Batzle, M., D. Han, and R. Hofmann (2006), Fluid mobility and frequency-dependent seismic velocity - Direct measurements, *Geophysics*, *71*(1), N1–N9.

Berkowitz, B. (2002), Characterizing flow and transport in fractured geological media: A review, *Adv. Water Resour.*, *25*(8), 861–884.

Biot, M. (1941), General theory of three-dimensional consolidation, *J. Appl. Phys.*, *12*, 155–164.

Biot, M. (1962), Mechanics of deformation and acoustic propagation in porous media, *J. Appl. Phys.*, *33*, 1482–1498.

Bordes, C., P. Sénéchal, J. Barrière, D. Brito, E. Normandin, and D. Jougnot (2015), Impact of water saturation on seismoelectric transfer functions: A laboratory study of coseismic phenomenon, *Geophys. J. Int.*, *200*(3), 1317–1335.

Carcione, J., and S. Picotti (2006), P-wave seismic attenuation by slow-wave difussion: Effects of inhomogeneous rock properties, *Geophysics*, *71*, O1–O8.

Caspari, E., T. Müller, and B. Gurevich (2011), Time-lapse sonic logs reveal patchy CO_2 saturation in-situ, *Geophys. Res. Lett.*, *38*, L13,301.

Clennell, M. B. (1997), Tortuosity: a guide through the maze, *Geol. Soc., London, Spec. Publ.*, *122*(1), 299–344.

Feynman, R. P., R. B. Leighton, M. Sands, and E. Hafner (1965), The Feynman lectures on physics, *Am. J. Phys.*, *33*(9), 750–752.

Grobbe, N., and E. Slob (2016), Seismo-electromagnetic thin-bed responses: Natural signal enhancements?, *J. Geophys. Res.*, *121*(4), 2460–2479.

Haartsen, M., and S. Pride (1997), Electroseismic waves from point sources in layered media, *J. Geophys. Res.*, *102*(B11), 24,745–24,769.

Haines, S. S., and S. R. Pride (2006), Seismoelectric numerical modeling on a grid, *Geophysics*, *71*(6), N57–N65.

Jardani, A., A. Revil, A. Bolève, A. Crespy, J. Dupont, W. Barrash, and B. Malama (2007), Tomography of the darcy velocity from self-potential measurements, *Geophys. Res. Lett.*, *34*(24), L24,403.

Jardani, A., A. Revil, E. Slob, and W. Söllner (2010), Stochastic joint inversion of 2D seismic and seismoelectric signals in linear poroelastic materials: A numerical investigation, *Geophysics*, *75*(1), N19–N31.

Jougnot, D., N. Linde, A. Revil, and C. Doussan (2012), Derivation of soil-specific streaming potential electrical parameters from hydrodynamic characteristics of partially saturated soils, *Vadose Zone J.*, *11*(1), doi:10.2136/vzj2011.0086.

Jougnot, D., J. G. Rubino, M. Rosas-Carbajal, N. Linde, and K. Holliger (2013), Seismoelectric effects due to mesoscopic heterogeneities, *Geophys. Res. Lett.*, *40*(10), 2033–2037.

Jougnot, D., N. Linde, E. Haarder, and M. Looms (2015), Monitoring of saline tracer movement with vertically distributed self-potential measurements at the HOBE agricultural test site, voulund, denmark, *J. Hydro.*, *521*(0), 314 – 327.

Jouniaux, L., and J. Pozzi (1995), Streaming potential and permeability of saturated sandstones under triaxial stress: Consequences for electrotelluric anomalies prior to earthquakes, *Journal of geophysical research*, *100*(B6), 10,197–10.

Jouniaux, L., and F. Zyserman (2016), A review on electrokinetically induced seismo-electrics, electro-seismics, and seismo-magnetics for earth sciences, *J. Geophys. Res.*, *7*(1), 249–284.

Krief, M., J. Garat, J. Stellingwerff, and J. Ventre (1990), A petrophysical interpretation using the velocities of P and S waves (full waveform inversion), *The Log Analyst*, *31*, 355–369.

Kruschwitz, S., A. Binley, D. Lesmes, and A. Elshenawy (2010), Textural controls on low-frequency electrical spectra of porous media, *Geophysics*, *75*(4), WA113–WA123.

Künze, R., P. Tomin, and I. Lunati (2014), Local modeling of instability onset for global finger evolution, *Adv. Water Resour.*, *70*, 148–159.

Linde, N., A. Binley, A. Tryggvason, L. Pedersen, and A. Revil (2006), Improved hydro-geophysical characterization using joint inversion of cross-hole electrical resistance and ground-penetrating radar traveltime data., *Water Resour. Res.*, *42*(12), W04,410.

Masson, Y., and S. Pride (2011), Seismic attenuation due to patchy saturation, *J. Geophys. Res.*, *116*, B03,206.

Masson, Y. J., and S. R. Pride (2007), Poroelastic finite difference modeling of seismic attenuation and dispersion due to mesoscopic-scale heterogeneity, *Journal of Geophysical Research: Solid Earth*, *112*(B3).

Mavko, G., T. Mukerji, and J. Dvorkin (2009), *The Rock Physics Handbook: Tools for Seismic Analysis of Porous Media*, Cambridge University Press.

Monachesi, L. B., J. G. Rubino, M. Rosas-Carbajal, D. Jougnot, N. Linde, B. Quintal, and K. Holliger (2015), An analytical study of seismoelectric signals produced by 1-D mesoscopic heterogeneities, *Geophys. J. Int.*, *201*(1), 329–342.

Müller, T., and B. Gurevich (2005), Wave-induced fluid flow in random porous media: Attenuation and dispersion of elastic waves, *J. Acoust. Soc. Amer.*, *117*, 2732–2741.

Müller, T., B. Gurevich, and M. Lebedev (2010), Seismic wave attenuation and dispersion resulting from wave-induced flow in porous rocks - A review, *Geophysics*, *75*, A147–A164.

Nakagawa, S., and M. Schoenberg (2007), Poroelastic modeling of seismic boundary conditions across a fracture, *J. Acoust. Soc. America*, *122*, 831–847.

Pimienta, L., J. Fortin, and Y. Guguen (2015), Bulk modulus dispersion and attenuation in sandstones, *GEOPHYSICS*, *80*(2), D111–D127, doi:10.1190/geo2014-0335.1.

Pride, S. (1994), Governing equations for the coupled electromagnetics and accoustics of porous media, *Phys. Rev.*, *50*(21), 15,678–15,696.

Revil, A., and A. Jardani (2009), Seismoelectric response of heavy oil reservoirs: theory and numerical modelling, *Geophys. J. Int.*, *180*(2), 781–797.

Revil, A., and P. Leroy (2004), Constitutive equations for ionic transport in porous shales, *J. Geophys. Res.*, *109*(B3), B03,208.

Revil, A., and N. Linde (2006), Chemico-electromechanical coupling in microporous media, *J. Coll. Interf. Sci.*, *302*(2), 682–694.

Revil, A., and H. Mahardika (2013), Coupled hydromechanical and electromagnetic disturbances in unsaturated porous materials, *Water Resour. Res.*, pp. 744–766, doi: 10.1002/wrcr.20092.

Revil, A., P. Pezard, and P. Glover (1999), Streaming potential in porous media: 1. theory of the zeta potential, *J. Geophys. Res.*, *104*(B9), 20,021–20,031.

Revil, A., A. Jardani, P. Sava, and A. Haas (2015), *The Seismoelectric Method: Theory and Application*, John Wiley & Sons.

Rubino, J., and K. Holliger (2012), Seismic attenuation and velocity dispersion in heterogeneous partially saturated porous rocks, *Geophys. J. Int.*, *188*, 1088–1102.

Rubino, J., C. Ravazzoli, and J. Santos (2009), Equivalent viscoelastic solids for heterogeneous fluid-saturated porous rocks, *Geophysics*, *74*, N1–N13.

Rubino, J., T. M. Müller, L. Guarracino, M. Milani, and K. Holliger (2014), Seismoacoustic signatures of fracture connectivity, *J. Geophys. Res.*, *119*(3), 2252–2271.

Rubino, J. G., C. L. Ravazzoli, and J. E. Santos (2006), Reflection and transmission of waves in composite porous media: A quantification of energy conversions involving slow waves, *J. Acoust. Soc. Am.*, *120*(5), 2425–2436.

Rubino, J. G., L. Guarracino, T. M. Müller, and K. Holliger (2013), Do seismic waves sense fracture connectivity?, *Geophys. Res. Lett.*, doi:10.1002/grl.50127.

Schakel, M., D. Smeulders, E. Slob, and H. Heller (2012), Seismoelectric fluid/porous-medium interface response model and measurements, *Transp. Por. Med.*, *93*(2), 271–282.

Sen, P. N., and P. A. Goode (1992), Influence of temperature on electrical conductivity on shaly sands, *Geophysics*, *57*(1), 89–96.

Sill, W. (1983), Self-potential modeling from primary flows, *Geophysics*, *48*(1), 76–86, doi:10.1190/1.1441409.

Solazzi, S. G., J. G. Rubino, T. M. Müller, M. Milani, L. Guarracino, and K. Holliger (2016), An energy-based approach to estimate seismic attenuation due to wave-induced fluid flow in heterogeneous poroelastic media, *Geophys. J. Int.*, *207*(2), 823–832.

Strahser, M., L. Jouniaux, P. Sailhac, P. Matthey, and M. Zillmer (2011), Dependence of seismoelectric amplitudes on water content, *Geophys. J. Int.*, *187*(3), 1378–1392.

Subramaniyan, S., B. Quintal, N. Tisato, E. H. Saenger, and C. Madonna (2014), An overview of laboratory apparatuses to measure seismic attenuation in reservoir rocks, *Geophys. Prospect.*, *62*(6), 1211–1223.

Suski, B., A. Revil, K. Titov, P. Konosavsky, M. Voltz, C. Dages, and O. Huttel (2006), Monitoring of an infiltration experiment using the self-potential method, *Water Resour. Res.*, *42*(8), W08,418.

Tardif, E., P. W. Glover, and J. Ruel (2011), Frequency-dependent streaming potential of ottawa sand, *J. Geophys. Res.*, *116*(B4).

Tisato, N., and C. Madonna (2012), Attenuation at low seismic frequencies in partially saturated rocks: Measurements and description of a new apparatus, *J. Appl. Geophys.*, *86*, 44–53.

Zhu, Z., and M. Toksöz (2005), Seismoelectric and seismomagnetic measurements in fractured borehole models, *Geophysics*, *70*(4), F45–F51, doi:10.1190/1.1996907.

Zyserman, F. I., P. M. Gauzellino, and J. E. Santos (2010), Finite element modeling of SHTE and PSVTM electroseismics, *J. Appl. Geophys.*, *72*(2), 79–91.

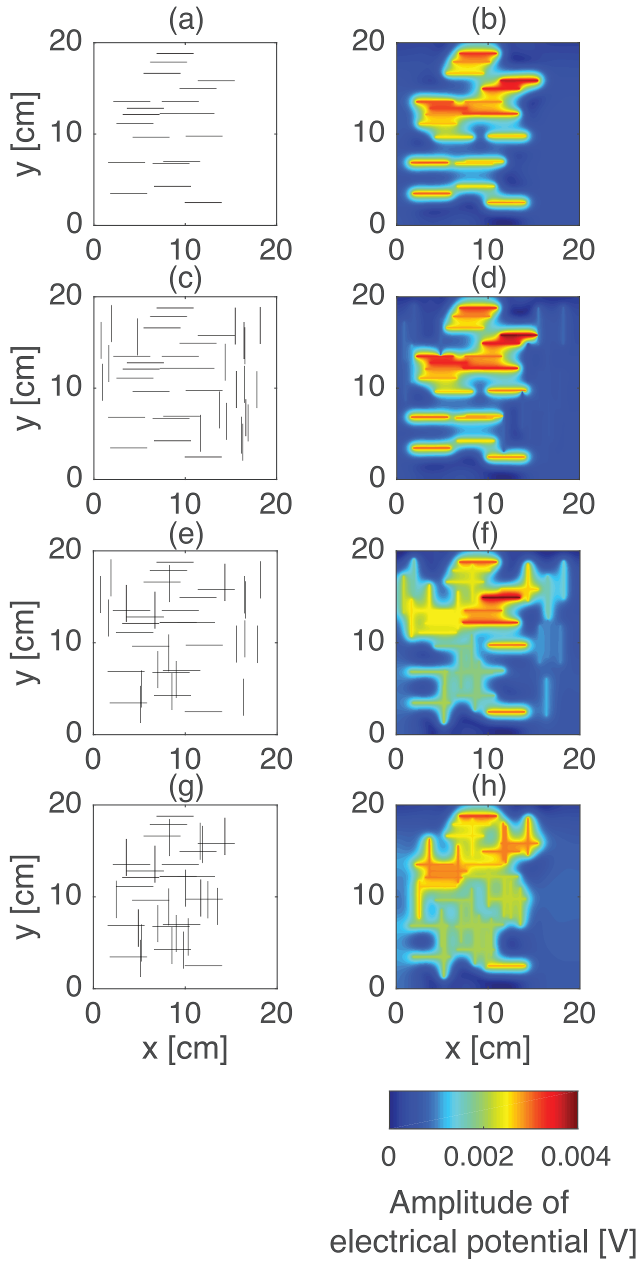

620 **Figure 12.** Left column: Rock samples used to test the effect of fracture connectivity on the seismoelectric signal. (a) Sample containing horizontal fractures that are not connected between each other. (c) Sample containing the same horizontal fractures as (a), plus vertical fractures, which are not connected to the horizontal ones. (e) Sample containing the same amount of horizontal and vertical fractures as in (c) but with some of the fractures connected. (g) Same as (b) but with every fracture connected. Right column: Amplitudes of the electrical potential in the samples shown in the left column for a frequency of 0.73 Hz.

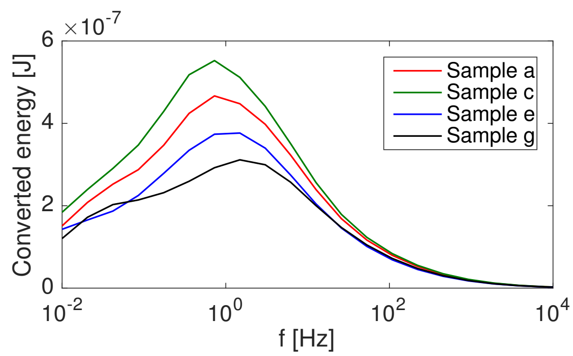

642 **Figure 13.** Total energy converted to seismoelectric signal in one period as a function of frequency for the
643 samples shown in Fig. 12a, c, e, and g.